nature electronics

Article

https://doi.org/10.1038/s41928-025-01406-1

An electro-optical Mott neuron based on niobium dioxide

Received: 30 March 2024

Accepted: 27 May 2025

Published online: 28 July 2025

Check for updates

Mahnaz Islam[1,2], Stephanie M. Bohaichuk[1], Timothy D. Brown[2], Sangheon Oh[2], Christopher Perez[2], Chengyang Zhang[3], Tae Joon Park[3,4], Minseong Park[2], A. Alec Talin[2], Shriram Ramanathan[3,7], Suhas Kumar[2,5] ✉ & Eric Pop[1,6] ✉

Various applications—including brain-like computing and on-chip artificial vision—increasingly demand a combination of electronic and photonic techniques. However, integrating both approaches on a single chip is challenging, and solutions typically rely on disparate components with power-hungry signal conversions. Here we report electro-optical Mott neurons that combine visible light emission with electrical threshold switching, as well as neuron-like oscillations. The devices are based on thin films of sputtered niobium dioxide (NbO_2), a Mott insulator–metal transition material, operating at room temperature and emitting light that peaks around 810 nm. Operando measurements reveal an electronic origin to the light emission: charge carrier relaxation initiated by high-field transport in the NbO_2. Our devices combine electrical and optical functions within a single material, thereby expanding the options available for future artificial intelligence hardware.

Brain-inspired hardware accelerators for artificial intelligence can exploit new electrical and optical processes to efficiently store and process complex information. Each of these two types of processes—electrical and optical—has its advantages. Electrical approaches using phase transitions can, for example, offer scalability and parallelism, whereas optical approaches can offer light-speed processing and high bandwidth[1]. Such computing is, however, increasingly focused on integrating many application-specific processors into single systems, with each processor handling different workloads matched to their advantages[2].

A neural network involves complex connections for both short- and long-range communications, which creates a challenge for conventional electrical interconnects. It is, thus, desirable to use optical interconnects for long-range communication due to its lower latency. Furthermore, in computer vision applications, it is desirable to combine visible-wavelength optical actuation and sensing with electrical processing on a single chip. However, it is typically inefficient to combine electronic and optical processors within a single system, let alone in dense, monolithically integrated circuits. Another difficulty in creating such electro-optical components is that light emission typically requires high-quality crystalline, epitaxial films, which are often incompatible with large-scale chip manufacturing. Therefore, common solutions rely on combining several discrete electrical and optical components, which incur considerable energy losses during electro-optical conversions.

In this article, we describe simultaneous electrical and optical functions in a single component built from sputtered niobium dioxide (NbO_2), a Mott insulator–metal-transition (IMT) material (Fig. 1). NbO_2, and other materials that undergo a phase change[3–9], can exhibit neuronal switching through a highly nonlinear current–voltage (I–V) characteristic, which can be used for brain-inspired computing[10]. Neuronal switching, in its simple form, is a volatile and abrupt change in resistance beyond a certain threshold voltage. Such devices display a region of steady-state S-type negative differential resistance (NDR)

[1]Electrical Engineering, Stanford University, Stanford, CA, USA. [2]Sandia National Laboratories, Livermore, CA, USA. [3]Materials Engineering, Purdue University, West Lafayette, IN, USA. [4]Department of Materials Science and Engineering, Korea University, Seoul, Republic of Korea. [5]Rain AI, San Francisco, CA, USA. [6]Materials Science and Engineering, Stanford University, Stanford, CA, USA. [7]Present address: School of Engineering, Rutgers University, Piscataway, NJ, USA. ✉e-mail: su1@alumni.stanford.edu; epop@stanford.edu

https://doi.org/10.1038/s41928-025-01406-1

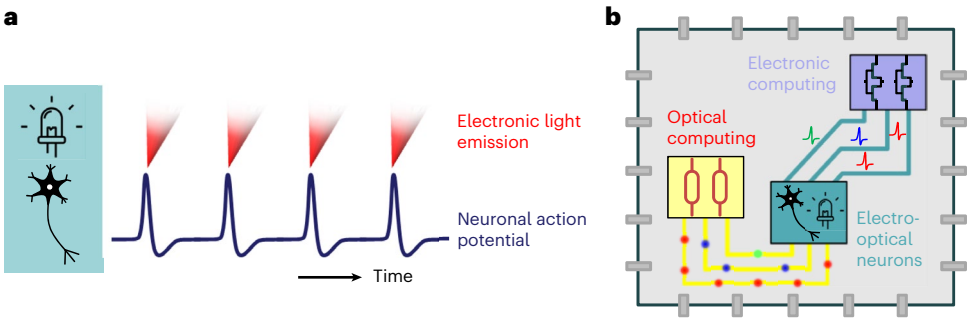

Fig. 1 | Electro-optic neuronal components. a, Illustration of combining neuronal behaviour and electronic light emission in a single component. **b**, Schematic of how a light-emitting electronic neuron can be used to integrate electronic and optical computing on a single monolithic circuit.

where the voltage decreases as the current increases. This effect has been used to create oscillatory neural networks and neuromorphic circuits that mimic the dynamic behaviour of biological neurons[11–13]. The underlying physics of resistive switching has been discussed in conjunction with the IMT that occurs at a critical temperature (1,080 K in NbO_2)[14,15], although the finer details of the microphysics, including the evolution of material properties throughout the transition, are still to be resolved.

We show that NbO_2 devices simultaneously emit visible light during resistive switching, a physically new phenomenon in Mott insulators. Furthermore, we also demonstrate simultaneous temporal dynamics of the neuron-like electrical self-oscillations, as well as oscillating (strobing) light emission from such devices. Although materials not typically associated with light emission can emit light by different physical mechanisms (including silicon, TaO_x and carbon-based nanostructures)[16–20], the threshold switching and NDR behaviour have not been known to simultaneously emit light in the same material[21–24]. We found that the origin of this light emission in NbO_2 is not due to black-body radiation from self-heating, but due to an electronic transition across an energy gap specific to the material. This demonstration of visible light emission in a single component made using an IMT material has potential applications in electro-optical computing, on-chip vision, metrology and on-chip light sources.

Light emission during threshold switching and oscillations

We fabricated lateral two-terminal NbO_2 devices (Fig. 2a) and applied dual voltage-controlled d.c. sweeps to obtain bipolar and volatile switching behaviour, as shown in Fig. 2b. The devices displayed abrupt, volatile current switching above a threshold voltage V_{IMT} (at point A). When the applied voltage V_s was increased (forward sweep), the device self-heated and underwent a Joule-heating-driven transition at V_{IMT}, resulting in a sharp decrease of the NbO_2 resistance and an abrupt increase of the device current (to point B). When V_s was decreased (reverse sweep) the device cooled down (to points C and D), resulting in increased NbO_2 resistance and a return to a high-resistance state (point E), with visible hysteresis during switching.

The physical origins of resistive switching in NbO_2 devices (driven by current or voltage) remain a topic of debate. The switching mechanism has been attributed to an IMT driven by Joule heating[3,25], analogous to the temperature-driven IMT at 1,080 K in crystalline NbO_2 films[15,26]. Other reports suggest that the switching is caused by nonlinear-transport-driven (for example, Poole–Frenkel) conduction coupled with Joule-heating-induced thermal runaway[4–6,8], which could initiate at as low as ~400 K in crossbar devices[8]. Nevertheless, most reports in the literature agree that Joule heating due to the applied bias plays an important role in NbO_2 resistive switching.

During the electrical measurements, we optically monitored the devices for signs of electrical breakdown but, instead, observed unexpected, bright visible light emission from the NbO_2 channel. The light surged during the A–B threshold switching (Fig. 2b,c) and then gradually decreased in magnitude for B–D. Our observation of light emission during switching from an IMT material may pave the way for an electro-optic neuronal component, as shown in Fig. 1. Optical images of an NbO_2 device at different bias levels are shown in Fig. 2c. Supplementary Video 1 shows light emission during the positive voltage sweep in Fig. 2b. The bottom panels of Fig. 2c plot the greyscale pixel intensity in the transverse direction across the NbO_2 channel for each bias state. The brightness ranged from 0 (black) to 255 (white).

The intensity of light emission was highest during threshold switching, possibly due to transient current overshoots during the abrupt resistance change (A–B). Light emission also occurred when the device was held in the low-resistance state (C–D), with an intensity proportional to the device current. The observed colour of the emission for a given device remained the same, irrespective of intensity. However, no light emission was observed in the high-resistance state (A or E) of the NbO_2 devices, regardless of the device current. We made similar observations for over 80 other NbO_2 devices with various film thickness (100 to 200 nm) across several chips, with consistent light emission and no breakdown noted, at least up to 50 cycles per device (Supplementary Fig. 1).

When biased with a current source (Supplementary Figs. 2–4), the devices displayed a region of S-type NDR after threshold switching, which was accompanied by self-sustaining current oscillations, as described in recent reports[11,27,28] for other IMT devices. The NbO_2 devices biased at increasing current values (I_{hold}) within the NDR region exhibited increasing frequencies of current oscillations (Supplementary Figs. 3 and 4). Other neuronal behaviours, such as frequency-dependent plasticity, pulse facilitation (potentiation and depression) and temporal learning have been shown in NbO_2 devices[11], demonstrating their scalability and integration potential for creating brain-inspired computing systems[29,30].

Figure 2d displays the electro-optical neuronal behaviour in our NbO_2 devices, as found by simultaneous electrical and optical measurements using the set-up in Supplementary Fig. 5 on a 5-µm-long device. An optical image and quasi-d.c. current and voltage sweeps are shown in the same supplementary figure. When biased in the NDR region at I_{hold} = 600 µA, the device displayed self-sustained current oscillations (blue, Fig. 2d), as expected. We found similar oscillations in the photodetector voltage measured concurrently (dark red, Fig. 2d). Thus, the device exhibited the electro-optical neuronal activity that we had predicted. Further measurements performed using this set-up are shown in Supplementary Fig. 6. On the other hand, Fig. 2e displays a systematic increase in the measured photodetector voltage when this device was biased at increasing current levels in the low-resistance state (like Fig. 2c), confirming the increase of light emission intensity with bias current in this state.

https://doi.org/10.1038/s41928-025-01406-1

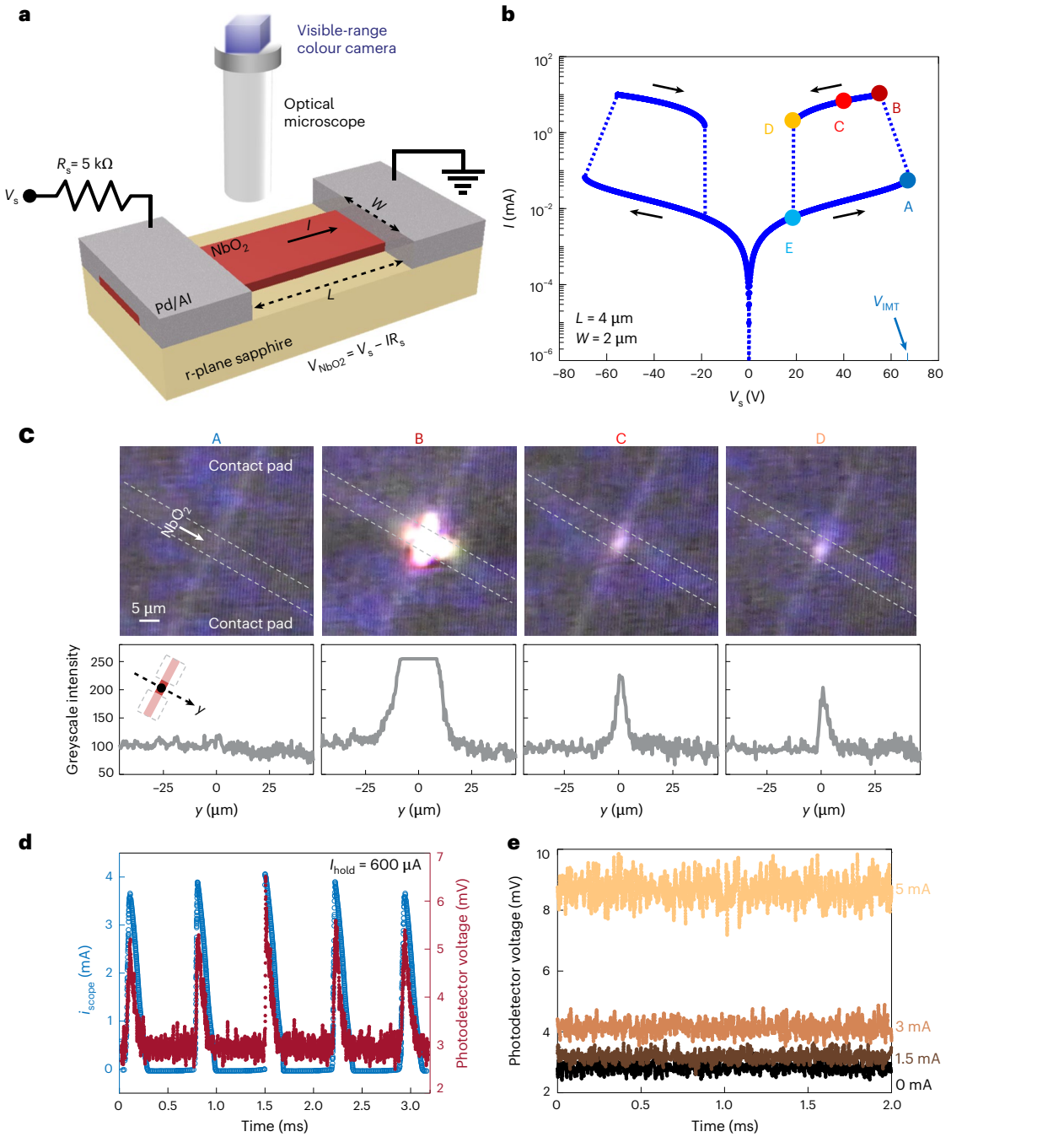

Fig. 2 | Light emission from NbO_2 devices. a, Device schematic showing electrical biasing and optical microscopy set-up.Here V_s, V_{NbO2}, I and R_s represent the supply voltage, device voltage, device current and series resistor, respectively. **b**, Bipolar and volatile switching measured in a 4-μm-long NbO_2 device. Arrows represent V_s sweep directions. A, high-resistance state; B, threshold switching (with transient overshoot); C,D, low-resistance state; E, return to high-resistance state. **c**, Operando images of a 5-μm-long NbO_2 device taken with the set-up in **a** at bias points A–D in **b**. Dashed lines mark the outline of the electrodes. Bottom panels show the greyscale pixel intensity in the transverse direction across the NbO_2 strip ($y \approx 0$ at the midpoint). Inset, bottom left panel, the y axis on a schematic of the device. A corresponding histogram of pixel counts versus greyscale intensity is shown in Supplementary Fig. 7. **d**, Simultaneous electronic and optical neuronal behaviour measured in a 5-μm-long NbO_2 device using the set-up in Supplementary Fig. 5a. Current oscillations (i_{scope}, blue) were measured with a 50-Ω oscilloscope in series with the device biased at a constant current (I_{hold} = 600 μA) in a region of NDR, as shown in Supplementary Fig. 5c. The corresponding photodetector voltage (dark red) measured concurrently across a 1-MΩ oscilloscope depicts the optical oscillations. **e**, Photodetector voltages measured when the NbO_2 device was off (I_{hold} = 0 mA) and when biased at increasing constant current (I_{hold} = 1.5, 3 or 5 mA, as labelled) in regions of low-resistance states where light emission was observed. Optical images (**c**) and photodetector voltages (**d**, **e**) were recorded with all ambient lights off.

We also performed simultaneous electrical characterization and optical microscopy of devices of various dimensions, using the set-up depicted in Fig. 2a. Although the colour of the light emission visually observed in the measured devices (on a single chip) remained invariant, the intensity of the observed emission was brighter for devices with longer channel lengths L (Supplementary Figs. 1 and 8). Devices with longer L have higher threshold voltages V_{IMT} and, thus, higher power dissipation during resistive switching. For example, devices with L from 2 to 5 μm switched at $V_{IMT} \approx 50$–90 V at ambient room temperature (Supplementary Fig. 8). The observed increase in

https://doi.org/10.1038/s41928-025-01406-1

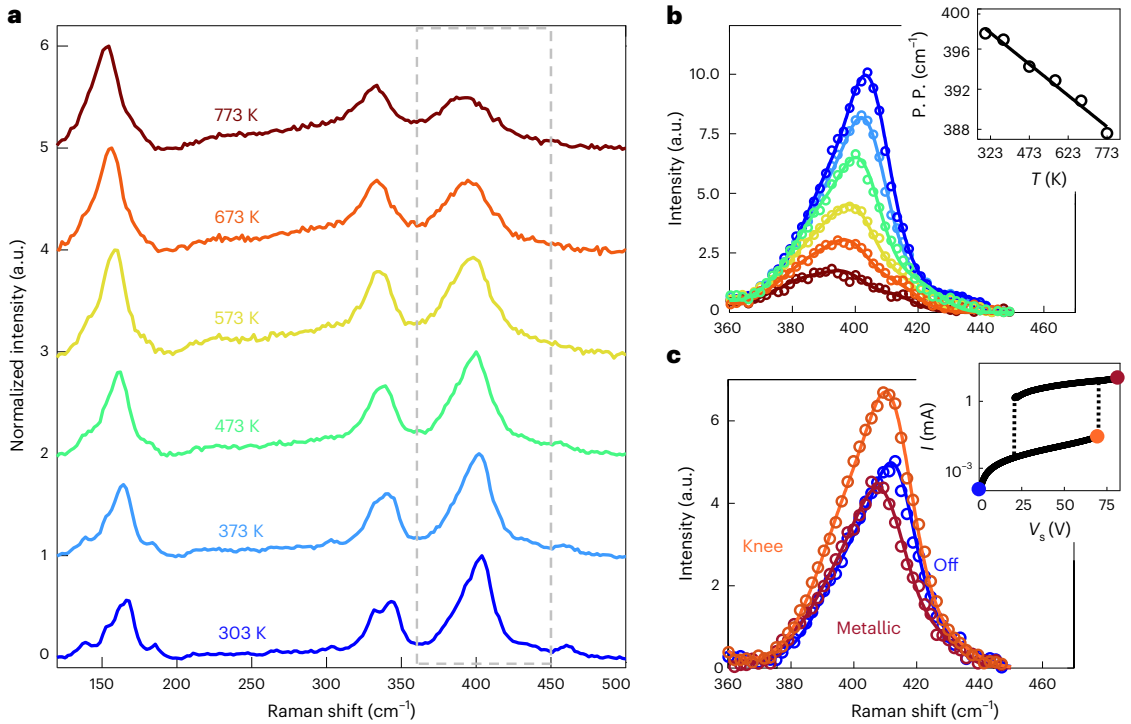

Fig. 3 | Raman thermometry of NbO_2 devices. a, Evolution of Raman spectra for 100-nm-thick NbO_2 films with increasing stage temperature. Each spectrum is normalized by its maximum value, and an arbitrary offset has been added for ease of plotting. **b**, Measured data (symbols) and fitted data (lines) for the Raman mode of the NbO_2 film near ~400 cm^{-1} (grey dashed box in **a**) used here for temperature calibration. The colours correspond to the temperatures in **a**. Inset, Raman peak position for the primary mode near 400 cm^{-1} versus stage temperature, depicting a redshift of -0.021 ± 0.004 cm^{-1} K^{-1} (complete peak decomposition is shown in Supplementary Fig. 17). **c**, Measured data (symbols) and fitted data (lines) for the Raman mode near ~400 cm^{-1} of a 5-μm-long NbO_2 device at different electrical biases, as shown in the inset, and referred to as the off, knee of the *I*–*V* curve and metallic bias states (full spectra and fitting in Supplementary Fig. 18). P. P., peak position.

V_{IMT} is consistent with previous measurements in similar materials[9], indicating that higher local heating and, thus, higher local temperatures are needed to increase the light emission intensity. This observation indicates that the light emission is tied to the Joule heating power, as we will discuss next.

The light emission was confined to near the middle of the channel (not along the edges), which was more apparent in the wider devices (Supplementary Fig. 9). This further confirms the importance of increased local temperatures for light emission because the maximum temperature is expected to form along the middle of the channel in an otherwise uniform IMT film[8,31]. (Our NbO_2 films were crystalline with grain sizes of the order of ~20 nm. The grains were much smaller than our device dimensions, so the heating patterns were like those in an otherwise uniform film[32].)

To check our understanding, we performed atomic force microscopy of the device channels before and after electrical switching. We noticed the formation of a permanent filament track ~300 nm wide after a single switching cycle, which was visible in both optical and atomic force microscopy images of the devices (Supplementary Fig. 10). The track marks the apparent current path formed between the electrodes. After several switching cycles, either the filament had grown wider or other distinct filaments had formed in the channel. These tracks mark irreversible changes in our devices and are possibly due to changes in microstructure or material recrystallization at the high local temperatures. These results are like reports for NbO_2 crossbars[8] and VO_2 (ref. 33) but are somewhat different from the reversible filaments discussed in studies that reported current focusing[5,7]. (Other devices measured at different ambient temperatures and with different channel lengths are shown in Supplementary Figs. 11 and 12.)

We also performed Raman spectroscopy measurements before and after the electrical switching, which did not show substantial changes in the Nb or O modes (Supplementary Fig. 13) and were consistent with NbO_2 (not Nb_2O_5). Elemental maps using energy-dispersive X-ray spectroscopy (Supplementary Fig. 14) did not uncover oxygen reduction (deficiency) after electrical switching. These findings are supported by the similar switching voltages in both bias polarities in Fig. 2b and Supplementary Fig. 1d. By contrast, O reduction would be expected to alter the device resistance after each switching event, leading to changes in the switching voltage.

Raman thermometry of NbO_2 devices

To estimate the local temperatures of the NbO_2 channel upon resistive switching, we performed Raman thermometry on our devices at various electrical biases of interest. Raman thermometry has previously been used to extract local temperatures during the operation of resistive memory[34] and transistor devices[35,36]. Although Raman spectroscopy of NbO_2 thin films under ambient conditions has been used to characterize film quality[37,38] and under a varying electrical bias to study phase transitions[39], in the present work, we used Raman thermometry to characterize local temperatures of NbO_2 resistive switching devices during operation.

To calibrate the Raman thermometry of NbO_2, we took temperature-dependent Raman spectra on a 100-nm-thick NbO_2 film, deposited under the same conditions as those used in our devices. These measurements were performed in $<10^{-4}$ Torr vacuum, given the tendency of NbO_2 to oxidize to Nb_2O_5 at higher ambient temperatures when exposed to air[40]. We confirmed the reversibility of the Raman measurements through heating and cooling cycles at elevated temperatures (Supplementary Fig. 15), which did not indicate that there were any

https://doi.org/10.1038/s41928-025-01406-1

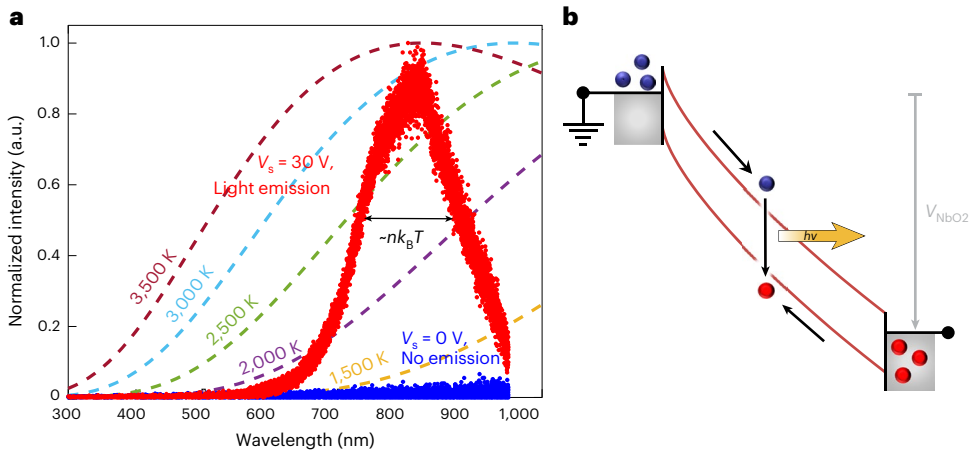

Fig. 4 | Emission spectroscopy of NbO_2 devices during operation. a, Light spectra emitted at visible wavelengths, measured operando at V_s = 30 V (red symbols) and 0 V (blue) for a 2-µm-long NbO_2 device. Dashed lines are calculated black-body spectra at various temperatures with an emissivity of unity. The emission peak was centred at 810 nm (1.53 eV) with FWHM ≈ nk_BT, where $3 < n < 9$, depending on whether an average or peak filamentary temperature of the NbO_2 was considered (see discussion in text). k_B is the Boltzmann constant. **b**, Energy band diagram of the proposed electroluminescence mechanism, which involves simultaneous majority (electron) and minority (hole) carrier injection at high field. V_{NbO_2} (= $V_s - IR_s \approx 5$ V) is the voltage across the NbO_2 device, after subtracting the series resistor R_s (see device layout in Fig. 2a). Diagram not to scale.

permanent changes over the temperature range used in the calibration. We also confirmed that the laser power used in this experiment (0.8 and 5.3 mW) did not cause substantial heating in the NbO_2 film (Supplementary Fig. 16) and did not introduce further Raman shifts.

As shown in Fig. 3a, the Raman spectrum for NbO_2 consists of low-frequency Nb modes below 200 cm^{-1} as well as a two-peak signature between 300 and 450 cm^{-1}, which are attributed to O-related phonons[40]. Increasing the stage temperature from 303 to 773 K caused an overall redshift of the Raman frequencies, as depicted in Fig. 3a. To quantify the redshifts, we decomposed the Raman peaks of interest at various temperatures (Supplementary Fig. 17) and show the temperature-dependence of the Raman mode near ~400 cm^{-1} in Fig. 3b. We used the primary mode near ~400 cm^{-1} in NbO_2 for thermometry, because only its peak position varied with temperature, as displayed in the inset of Fig. 3b. We found with a linear fit that the redshift rate with temperature of this mode was -0.021 ± 0.004 cm^{-1} K^{-1}.

Next, we performed Raman spectroscopy on a 5-µm-long NbO_2 device with different electrical biases. Figure 3c shows the resulting Raman mode near ~400 cm^{-1} (chosen for thermometry as explained previously), with data marked in blue corresponding to the unbiased device (labelled 'off'), orange to the high-resistance state just before the threshold switching ('knee') and dark red to the low-resistance state ('metallic') where light emission is observed. We calculated the shift of the primary mode (Supplementary Fig. 18b) for the two bias states relative to the unbiased state and estimated the in situ temperatures using the calibration from Fig. 3b. The results are summarized in Supplementary Table 2, which shows that, at the knee in Fig. 3c, the NbO_2 channel heated up to 69 ± 13 K, on average, above room temperature just before threshold switching. Thus, resistive switching in our device initiated at <375 K, much below the reported Mott transition for NbO_2 at 1,080 K. However, our finding is consistent with previous work that estimated threshold switching near ~400 K in NbO_2 devices[8]. Looking at the low-resistance state (metallic), where light emission is observed, the Raman measurement indicates that the NbO_2 channel reached 201 ± 38 K above room temperature. The measured maximum device temperature (~530 K) was too low for the observed visible light to be driven by NbO_2 black-body radiation, as discussed in 'Spectroscopy of observed light emission'.

Note that the Raman measurements estimate a temperature averaged across the ~1-µm-wide laser spot size. However, NbO_2 switching appears to occur in filamentary tracks as narrow as ~300 nm, as shown in Supplementary Fig. 10 and discussed earlier. To estimate the localized temperatures within these tracks, we carried out finite-element simulations, as described in Supplementary Information Section 6. These results indicate that the temperature of such filaments could reach ~1,250 K, which is above the Mott transition in NbO_2 but not sufficiently high to drive strong black-body emission and account for the visible light we observed in our devices.

Spectroscopy of observed light emission

To identify the physical origins of the light emission, we performed in situ emission microscopy of the NbO_2 devices in the visible range, using a set-up like the one in Fig. 2a. A 2-µm-long NbO_2 device (chosen because it has lower V_{IMT}) was held at 30 V d.c. bias in its low-resistance, light-emitting state, like B in Fig. 2b,c. The measured spectrum of the emitted light is marked by the red symbols in Fig. 4a. This spectrum had a strong peak at 810 nm, with significant emission through Stanford Cardinal red (~750 nm) and into the orange wavelengths of the visible spectrum[41], down to about 600 nm.

Dashed lines in Fig. 4a represent our calculations with a pure black-body radiation model (with an emissivity of 1) at various temperatures. However, none of them can explain the measured light emission from our NbO_2 devices. A black-body emission peak centred around our experimental data would require a temperature of 3,500 K, much higher than any temperatures estimated under even the highest bias conditions in our NbO_2 devices. Such a temperature is also beyond the melting point of NbO_2 (~2,190 K) and of the contact metals (~1,825 K for Pd and ~930 K for Al) in our devices, rendering it implausible.

Note that the emission peak at 810 nm corresponds to an energy of 1.53 eV. For NbO_2 in the insulating state, a range of bandgap energies has been reported[14,42–48] from 0.5 to 1.6 eV, depending on the measurement or computational technique and on the crystallinity or phase purity of the material (for example, NbO_2 versus Nb_2O_5). (The indirect bandgap was estimated to be lower than the direct gap within the measurement range[46,48].) However, our observed transition energy was notably close to the $d_{||}$–e_g^{π} orbital splitting of 1.58 eV reported by Wong et al.[44] in NbO_2 films prepared on sapphire using the same deposition method as in our work. Light emission was undetectable in the high-resistance state, where current levels were over two orders of magnitude lower.

Based on the above arguments, we, thus, propose an electroluminescence mechanism that relies on electron–hole recombination

across an ~1.53 eV (810 nm) energy gap in these NbO_2 devices. Light emission was observable only in the low-resistance state, in part due to the much higher current (greater free carrier densities available) and in part due to the high electric field and device self-heating, which enabled minority carrier injection (Fig. 4b). The electroluminescence peak had a full-width at half-maximum, FWHM ≈ nk_BT, where $3 < n < 9$, with the lower bound corresponding to the (peak) localized temperature estimated by our simulations of filamentary heating in NbO_2 (Supplementary Information Section 6) and the upper bound given by the (average) temperature of ~400 K based on our Raman thermometry measurements. Regardless, this range is broader than the theoretically expected $1.8k_BT$ for spontaneous light emission in a parabolic-band semiconductor[49], most probably due to intrinsic defects in our films.

To understand the conversion between electrical input power and optical output power of our NbO_2 devices, we calibrated our spectrometer response using a standard 780-nm light-emitting diode under the same conditions as in our emission measurements (Supplementary Fig. 20). For an electrical power input of ~24.5 mW, we estimated an optical power output of ~0.2 μW (~10^{12} photons per second), corresponding to the peak intensity counts at 816 nm for the device in Fig. 4a. Note that this is an estimate only of the electro-optical conversion efficiency at the peak wavelength and is not intrinsically limited. Future work could include device and materials engineering to improve the conversion efficiency, for example, by passivating defects, introducing luminescence centres for variable emission wavelengths and optical engineering to improve light extraction efficiency.

Conclusions

We have shown that visible light can be emitted during neuronal switching in NbO_2 devices, under the same conditions that drive NDR and self-oscillations. This was surprising, because neuron-like switching is not typically associated with optical activity in semiconductor electronics. The light emission peak occurred near 810 nm in the low-resistance state. Raman thermometry and electro-thermal simulations indicated that the NbO_2 temperature during switching was not sufficiently high to support pure black-body-driven light emission at visible wavelengths. Instead, emission spectroscopy pointed to an electronic transition across an energy gap of 1.53 eV assisted by the high-field injection of minority carriers (holes) into an otherwise n-type material.

This demonstration of simultaneous electrical and optical functions in a single component using neuronal switching in NbO_2 could potentially lead to new metrology approaches for correlated electron systems and electro-optical neuronal components that do not rely on power-expensive domain conversions. For example, in heterogeneous systems that include both electronic and optical components, such electro-optical Mott neurons could enable long-distance, interneuron signalling using optical pulses (which minimize latency), while encoding their state in the electrical response (which can be recorded and stored). Future studies could examine the integration of such NbO_2 switches[11,50,51], including light emission and signalling between scaled devices.

Methods

Device fabrication

Crystalline NbO_2 films of thickness 100, 150 or 200 nm were grown on 1 cm × 1 cm r-plane sapphire substrates (of 0.5 mm or 1 mm thickness) using an AJA ultra-high-voltage magnetron sputtering system at a deposition temperature[52] of 750 °C. NbO_2 channels of widths $W = 2$ to 25 μm and lengths $L = 1.5$ to 8 μm were patterned by optical lithography followed by CF_4/Ar dry etching (60 sccm CF_4, 30 sccm Ar, 5 mTorr, 500 W inductively coupled plasma power, 100 W bias power and ~90 nm min^{-1} etch rate), followed by electron-beam evaporation and photoresist-assisted lift-off of Pd (100 nm)/Al (400 nm) contacts.

Electrical and optical characterization

All electrical measurements were performed using a Keithley 4200-SCS parameter analyser as a current or voltage source on a micromanipulator probe station from Janis Research under vacuum at <10^{-4} Torr. All devices were measured with a series resistor $R_s = 5$ kΩ to prevent failure due to transient overshoots during switching. A 10-mA current compliance was set in the parameter analyser. Current oscillations were measured using an Agilent InfiniiVision MSO710A oscilloscope with a 50-Ω input impedance in series with the device. All optical microscopy images were captured using a visible-range charge-coupled device (CCD) colour camera. Optical oscillations were measured using an ultrasensitive Si photomultiplier. More details of each of these measurement set-ups can be found in Supplementary Information Sections 1, 2 and 3.

Raman thermometry measurements

All measurements described in 'Raman thermometry of NbO_2 devices' were performed using a Renishaw InVia Reflex spectrometer (532 nm laser, 50 mW total laser power, 100 cm^{-1} edge filter, 1,800 lines per millimetre grating and laser spot size ~1 μm). The temperature-controlled Raman measurements were performed using a Nextron thermal stage equipped with a sapphire optical window under continuous vacuum at <10^{-4} Torr with 5.3 mW laser power, 5 s acquisition time and 35 accumulations. The bias-controlled Raman measurements were performed using a Nextron microprobe system under vacuum at <10^{-4} Torr with a 5-kΩ series resistor on wire-bonded NbO_2 devices while the laser power was decreased to 0.8 mW with 25 accumulations. More details about this measurement set-up can be found in Supplementary Information Section 5. Further Raman spectroscopy measurements made with a HORIBA instrument are described in Supplementary Information Section 4.

Emission spectroscopy

NbO_2 devices were wire-bonded and biased using a Nextron microprobe system under vacuum at <10^{-4} Torr with a 5-kΩ resistor in series. The resulting light emission was captured through a Renishaw InVia confocal microscope (×50 objective) and analysed using a Reflex spectrometer coupled with a Peltier-cooled deep depletion CCD detector (1,800 lines per millimetre grating, 10 s acquisition time and two accumulations).

Peak-fitting

All peaks were fitted using a Gaussian (amplitude) distribution in Peakfit v4.12.

Data availability

The data that support the plots within this paper and other findings of the study are available from the corresponding authors upon request.

References

1. Emboras, A. et al. Opto-electronic memristors: prospects and challenges in neuromorphic computing. *Appl. Phys. Lett.* **117**, 230502 (2020).
2. Kendall, J. D. & Kumar, S. The building blocks of a brain-inspired computer. *Appl. Phys. Rev.* **7**, 011305 (2020).
3. Pickett, M. D. & Williams, R. S. Sub-100 fJ and sub-nanosecond thermally driven threshold switching in niobium oxide crosspoint nanodevices. *Nanotechnology* **23**, 215202 (2012).
4. Slesazeck, S. et al. Physical model of threshold switching in NbO_2 based memristors. *RSC Adv.* **5**, 102318–102322 (2015).
5. Gibson, G. A. et al. An accurate locally active memristor model for S-type negative differential resistance in NbO_x. *Appl. Phys. Lett.* **108**, 023505 (2016).
6. Funck, C. et al. Multidimensional simulation of threshold switching in NbO_2 based on an electric field triggered thermal runaway model. *Adv. Electron. Mater.* **2**, 1600169 (2016).

7. Li, S., Liu, X. J., Nandi, S. K. & Elliman, R. G. Anatomy of filamentary threshold switching in amorphous niobium oxide. *Nanotechnology* **29**, 375705 (2018).
8. Kumar, S. et al. Physical origins of current and temperature controlled negative differential resistances in NbO_2. *Nat. Commun.* **8**, 658 (2017).
9. Bohaichuk, S. M. et al. Localized triggering of the insulator-metal transition in VO_2 using a single carbon nanotube. *ACS Nano* **13**, 11070–11077 (2019).
10. Zhou, Y. & Ramanathan, S. Mott memory and neuromorphic devices. *Proc. IEEE* **103**, 1289–1310 (2015).
11. Kumar, S., Williams, R. S. & Wang, Z. W. Third-order nanocircuit elements for neuromorphic engineering. *Nature* **585**, 518–523 (2020).
12. Kim, G. M. et al. Self-clocking fast and variation tolerant true random number generator based on a stochastic Mott memristor. *Nat. Commun.* **12**, 2906 (2021).
13. Weiher, M. et al. Improved vertex coloring with NbO_x memristor-based oscillatory networks. *IEEE Trans. Circuits Syst. I: Regul. Pap.* **68**, 2082–2095 (2021).
14. Sakai, Y., Tsuda, N. & Sakata, T. Electrical properties of semiconducting NbO_2. *J. Phys. Soc. Jpn* **54**, 1514–1518 (1985).
15. Seta, K. & Naito, K. Calorimetric study of the phase-transition in doped NbO_2. *J. Chem. Thermodyn.* **14**, 937–949 (1982).
16. Fauchet, P. M. Light emission from Si quantum dots. *Mater. Today* **8**, 26–33 (2005).
17. Zhu, M. M., Zhang, Z. J. & Miao, W. Intense photoluminescence from amorphous tantalum oxide films. *Appl. Phys. Lett.* **89**, 021915 (2006).
18. Kim, Y. D. et al. Bright visible light emission from graphene. *Nat. Nanotechnol.* **10**, 676–681 (2015).
19. Mann, D. et al. Electrically driven thermal light emission from individual single-walled carbon nanotubes. *Nat. Nanotechnol.* **2**, 33–38 (2007).
20. He, C. L. et al. Tunable electroluminescence in planar graphene/SiO_2 memristors. *Adv. Mater.* **25**, 5593–5598 (2013).
21. Shan, L. T. et al. Artificial tactile sensing system with photoelectric output for high accuracy haptic texture recognition and parallel information processing. *Nano Lett.* **22**, 7275–7283 (2022).
22. Zhu, Y. B. et al. Light-emitting memristors for optoelectronic artificial efferent nerve. *Nano Lett.* **21**, 6087–6094 (2021).
23. Shan, L. T. et al. A sensory memory processing system with multi-wavelength synaptic-polychromatic light emission for multi-modal information recognition. *Nat. Commun.* **14**, 2648 (2023).
24. Chen, Z. J. et al. Cross-layer transmission realized by light-emitting memristor for constructing ultra-deep neural network with transfer learning ability. *Nat. Commun.* **15**, 1930 (2024).
25. Liu, X. J., Li, S., Nandi, S. K., Venkatachalam, D. K. & Elliman, R. G. Threshold switching and electrical self-oscillation in niobium oxide films. *J. Appl. Phys.* **120**, 124102 (2016).
26. Janninck, R. F. & Whitmore, D. H. Electrical conductivity and thermoelectric power of niobium dioxide. *J. Phys. Chem. Solids* **27**, 1183–1187 (1966).
27. Bohaichuk, S. M. et al. Intrinsic and extrinsic factors influencing the dynamics of VO_2 Mott oscillators. *Phys. Rev. Appl.* **19**, 044028 (2023).
28. Yi, W. et al. Biological plausibility and stochasticity in scalable VO_2 active memristor neurons. *Nat. Commun.* **9**, 4661 (2018).
29. Liu, J. Q. et al. A bioinspired flexible neuromuscular system based thermal-annealing-free perovskite with passivation. *Nat. Commun.* **13**, 7427 (2022).
30. Ni, Y. et al. Visualized in-sensor computing. *Nat. Commun.* **15**, 3454 (2024).
31. Nandi, S. K. et al. High spatial resolution thermal mapping of volatile switching in NbO_x-based memristor using in situ scanning thermal microscopy. *ACS Appl. Mater. Interfaces* **14**, 29025–29031 (2022).
32. del Valle, J. et al. Spatiotemporal characterization of the field-induced insulator-to-metal transition. *Science* **373**, 907–911 (2021).
33. Jeong, J. H. et al. Current induced polycrystalline-to-crystalline transformation in vanadium dioxide nanowires. *Sci. Rep.* **6**, 37296 (2016).
34. Yalon, E. et al. Spatially resolved thermometry of resistive memory devices. *Sci. Rep.* **7**, 15360 (2017).
35. Yalon, E. et al. Energy dissipation in monolayer MoS_2 electronics. *Nano Lett.* **17**, 3429–3433 (2017).
36. Kuball, M. & Pomeroy, J. W. A review of Raman thermography for electronic and opto-electronic device measurement with submicron spatial and nanosecond temporal resolution. *IEEE Trans. Device Mater. Reliab.* **16**, 667–684 (2016).
37. Shibuya, K. & Sawa, A. Epitaxial growth and polarized Raman scattering of niobium dioxide films. *AIP Adv.* **12**, 055103 (2022).
38. Zhao, Y., Zhang, Z. J. & Lin, Y. H. Optical and dielectric properties of a nanostructured NbO_2 thin film prepared by thermal oxidation. *J. Phys. D* **37**, 3392–3395 (2004).
39. Fakih, A., Shinde, O., Biscaras, J. & Shukla, A. Raman evidence for absence of phase transitions in negative differential resistance thin film devices of niobium dioxide. *J. Appl. Phys.* **127**, 084503 (2020).
40. Fajardo, G. J. P. et al. Structural phase transitions of NbO_2: bulk versus surface. *Chem. Mater.* **33**, 1416–1425 (2021).
41. Sliney, D. H. What is light? The visible spectrum and beyond. *Eye* **30**, 222–229 (2016).
42. Adler, D. Mechanisms for metal-nonmetal transitions in transition-metal oxides and sulfides. *Rev. Mod. Phys.* **40**, 714–736 (1968).
43. Lee, J. C. & Durand, W. W. Electrically stimulated optical switching of NbO_2 thin films. *J. Appl. Phys.* **56**, 3350–3352 (1984).
44. Wong, F. J., Hong, N. N. & Ramanathan, S. Orbital splitting and optical conductivity of the insulating state of NbO_2. *Phys. Rev. B* **90**, 115135 (2014).
45. Posadas, A. B., O'Hara, A., Rangan, S., Bartynski, R. A. & Demkov, A. A. Band gap of epitaxial in-plane-dimerized single-phase NbO_2 films. *Appl. Phys. Lett.* **104**, 092901 (2014).
46. O'Hara, A., Nunley, T. N., Posadas, A. B., Zollner, S. & Demkov, A. A. Electronic and optical properties of NbO_2. *J. Appl. Phys.* **116**, 213705 (2014).
47. Stoever, J. et al. Approaching the high intrinsic electrical resistivity of NbO_2 in epitaxially grown films. *Appl. Phys. Lett.* **116**, 182103 (2020).
48. Kulmus, K., Gemming, S., Schreiber, M., Pashov, D. & Acharya, S. Theoretical evidence for the Peierls transition in NbO_2. *Phys. Rev. B* **104**, 035128 (2021).
49. Schubert, E. F. *Light-Emitting Diodes* (Cambridge Univ. Press, 2006).
50. Kim, G. et al. Mott neurons with dual thermal dynamics for spatiotemporal computing. *Nat. Mater.* **23**, 1237–1244 (2024).
51. Zhang, X. M. et al. An artificial spiking afferent nerve based on Mott memristors for neurorobotics. *Nat. Commun.* **11**, 51 (2020).
52. Wong, F. J. & Ramanathan, S. Heteroepitaxy of distorted rutile-structure WO_2 and NbO_2 thin films. *J. Mater. Res.* **28**, 2555–2563 (2013).

Acknowledgements

Part of this work was performed at the Stanford Nanofabrication Facility and Stanford Nano Shared Facilities, which are supported by the National Science Foundation (Award No. ECCS-026822). This work was supported as part of the Center for Reconfigurable Electronic Materials Inspired by Nonlinear Neuron Dynamics (reMIND), an Energy Frontier Research Center funded by the US Department of Energy, Office of Science, Basic Energy Sciences. The Laboratory Directed R&D programme of Sandia National Laboratories provided internal support to the reMIND Energy Frontier Research Center. M.I., T.D.B., S.O., A.A.T. and S.K. were partially supported by reMIND. C.P. and M.P.

were partially supported by the Laboratory Directed R&D programme. M.I. and S.M.B. were partially supported by the Stanford Graduate Fellowship Program. S.R. acknowledges support from the Air Force Office of Scientific Research (Grant No. FA9550-18-1-0250). E.P. acknowledges partial support from the Stanford SystemX Alliance. This paper describes objective technical results and analyses. Any subjective views or opinions that might be expressed in the paper do not necessarily represent the views of the US Department of Energy or the US Government.

Author contributions

M.I., S.M.B., S.K. and E.P. conceived the idea. M.I. performed all electrical characterization and electro-optical microscopy measurements. S.M.B. fabricated the NbO_2 devices and first observed light emission. M.I. and S.M.B. performed all materials characterizations. M.I. and T.D.B. performed the Raman thermometry and emission spectroscopy measurements with advice from A.A.T. and S.K. M.I. and S.O. measured simultaneous electro-optical activity with advice from A.A.T. C.P. wire-bonded NbO_2 devices and assisted with Raman thermometry and emission spectroscopy measurements. C.Z. and T.J.P. grew the NbO_2 films with advice from S.R. S.M.B. and M.P. performed the electro-thermal simulations. M.I. analysed all the data and wrote the manuscript with help from S.K. and E.P. All authors have given approval to the final version of the manuscript.

Competing interests

The authors declare no competing interests.

Additional information

Supplementary information The online version contains supplementary material available at https://doi.org/10.1038/s41928-025-01406-1.

Correspondence and requests for materials should be addressed to Suhas Kumar or Eric Pop.

Peer review information *Nature Electronics* thanks Kyung Min Kim, Juan Gabriel Ramírez and Wentao Xu for their contribution to the peer review of this work.

nature electronics

Supplementary information

https://doi.org/10.1038/s41928-025-01406-1

An electro-optical Mott neuron based on niobium dioxide

In the format provided by the authors and unedited

Table of Contents:

1. Measurement Setup for Quasi-DC and Oscillatory Behavior

Electrical measurements were performed under vacuum at $<10^{-4}$ Torr in a micromanipulator probe station from Janis Research with a Keithley 4200-SCS parameter analyzer as a current/voltage source. When used as a current source, measurements were performed using either the "fast" or "normal" speed mode. Unless otherwise mentioned, all measurements were done at room temperature ambient (~293 K) and with a 5.1 kΩ resistor added in series to the device (on the probe arm) as a current compliance. This protects devices from failure during the resistive switching and prevents transient current (power) overshoots. A 10 mA current compliance was also set in the parameter analyzer for all measurements. Current oscillations were measured using an Agilent InfiniiVision MSO710A oscilloscope with a 50 Ω input series impedance.

Supplementary Fig. S1 represents multiple dual voltage-controlled sweeps performed on our NbO_2 devices across different dimensions and chips. No device degradation was observed in any device up to the number of voltage-controlled sweeps performed for each. Light emission was observed in all devices upon each switching in **Supplementary Figs. S1a**, **b**, and **d**. The observed emission appears brighter for devices with longer channel lengths, L (**Supplementary Figs. S1b** and **d**), as discussed in main text and further shown in **Supplementary Fig. S8**. While light emission of varying brightness was consistently observed during repeated resistive switching in devices of all widths with $L \geq 2$ μm, for $L \approx 1.5$ μm (the shortest device measured in this work, **Supplementary Fig. S1c**), we find that very weak light emission could still be detected in the narrower channels ($W \leq 15$ μm) in each cycle (up to 20 cycles performed for each) but was undetectable in the widest channels with $W \geq 20$ μm (black and greys), even though all devices had comparable switching voltages, V_{IMT}. The slight variation in switching voltages may be due to the slight variation in channel lengths patterned by lithography. This could be a limitation of our optical microscopy detection technique (*i.e.*, emitted light intensity in the widest devices with $L \approx 1.5$ μm is below the detection limit of our visible-range camera).

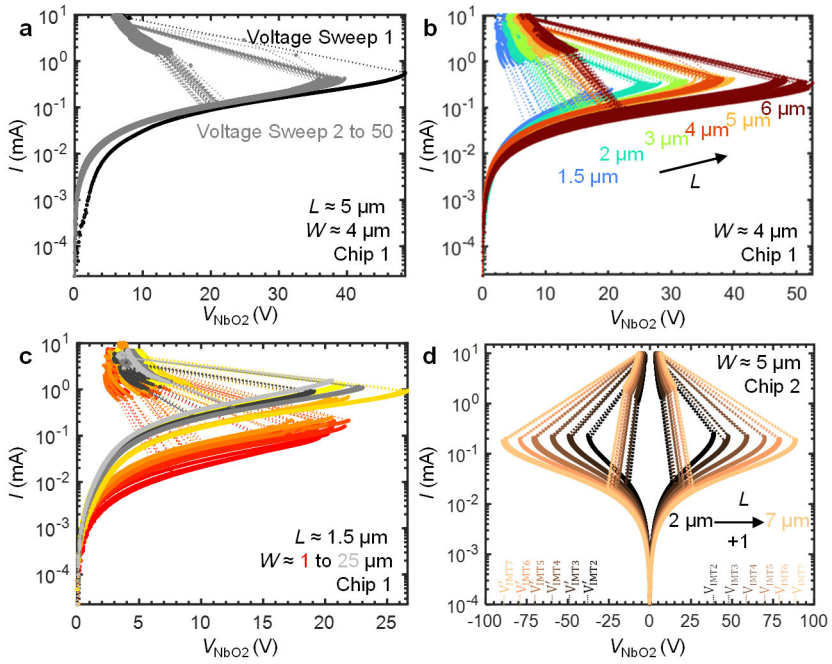

Fig. S1. Stability of NbO_2 devices and repeatability of electro-optical light emission. **a,** 50 dual voltage-controlled sweeps performed on an NbO_2 device. Sweeps 2 to 50 are in gray. A small burn-in was observed *only* after the first voltage sweep (black), similar to all devices measured in this work. **b,** 30 dual voltage-controlled sweeps performed (sweep 1 is *not* shown) on 4 µm wide devices with varying channel lengths ($L \approx 1.5$ to 6 µm, as labeled). **c,** 5 dual voltage-controlled sweeps performed on NbO_2 devices with $L \approx 1.5$ um and varying widths $W \approx 1$ µm (red) to 25 µm (light grey). **d,** 5 bipolar and dual voltage-controlled sweeps performed on 4 µm wide devices with varying channel lengths ($L \approx 2$ to 7 µm, as labeled). V_{IMT} and V'_{IMT} represent the switching voltages for positive and negative voltage-controlled sweeps, respectively, for each L (as labeled). Measurements shown in **a**, **b**, and **c** are on chip 1 (150 nm thick NbO_2 film on 0.5 mm sapphire substrate) and those in **d** are on chip 2 (100 nm thick NbO_2 film on 1 mm sapphire substrate), hence the difference in switching voltages (V_{IMT}) between devices with similar L.

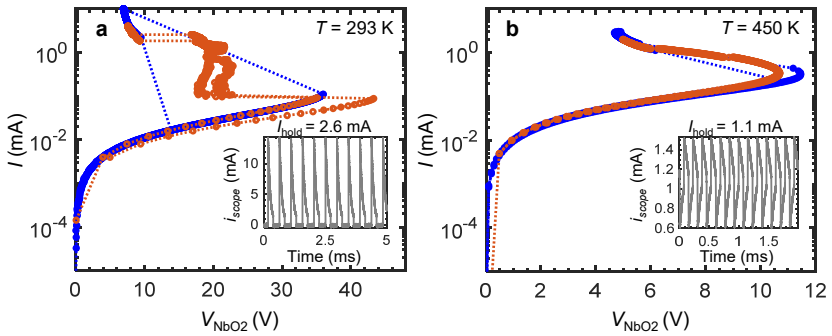

Fig. S2. Quasi-DC switching in NbO_2 measured via dual voltage-controlled sweeps (blue) and current-controlled sweeps (red, in slow measurement mode) at different ambient temperatures. **a,** 4 (L) × 8 (W) µm device measured at 293 K and **b,** 2 (L) × 1.5 (W) µm device measured at 450 K. The inset shows the oscillations in current measured when the device is biased with a constant current (I_{hold}) in a region of negative differential resistance (NDR).

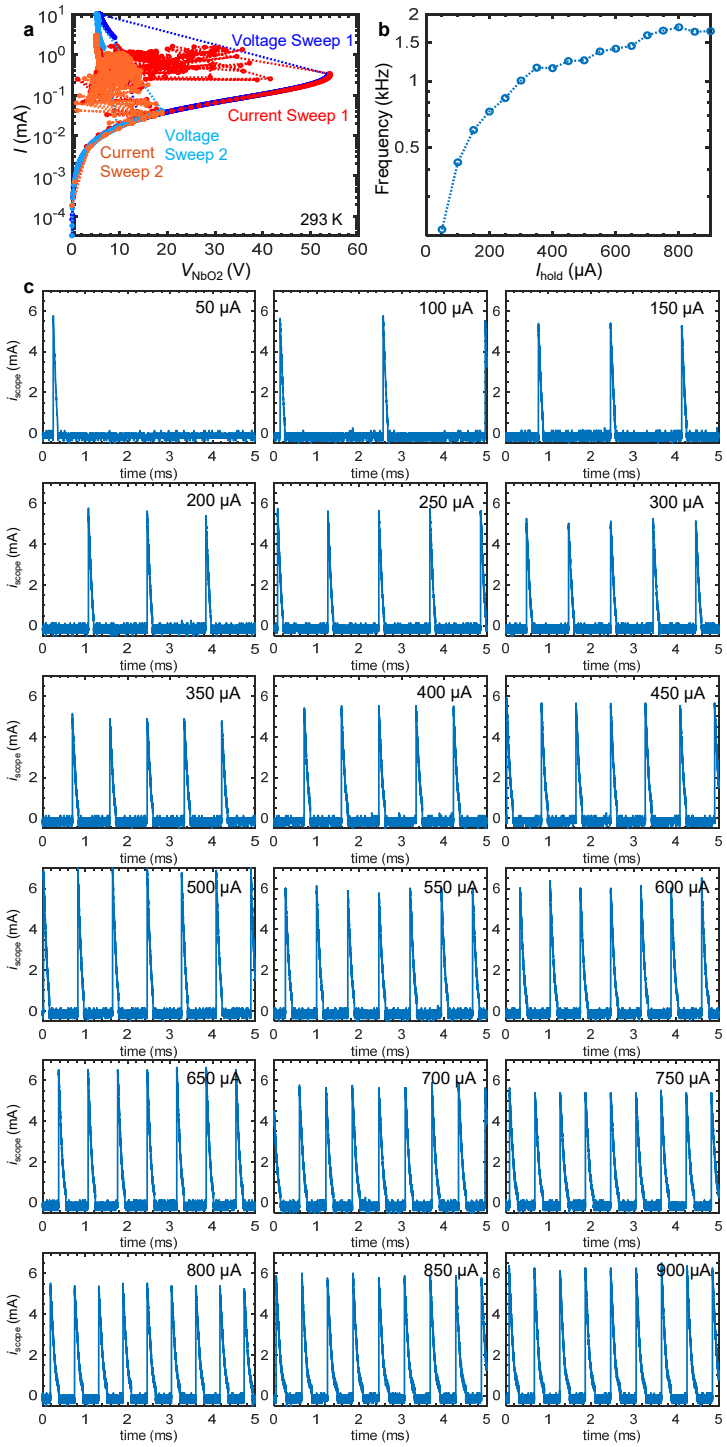

Fig. S3. Current oscillations measured in a 4 (L) × 10 (W) μm NbO_2 device at room temperature ambient with a 2 kΩ compliance resistor. **a,** Quasi-DC switching measured via dual voltage-controlled sweeps (blue and light blue) and current-controlled sweeps (red and orange, in fast measurement mode). Voltage sweep 1 (blue) is performed in the pristine state and voltage sweep 2 (light blue) is measured after performing current sweep 1 (red), showing huge burn-in in the device switching voltage when current-controlled sweeps are performed at room temperature ambient. **b,** Oscillation frequency versus current value (I_{hold}) when the device is held in different regions within the NDR state. **c,** Corresponding current oscillations measured in the device at different current values, I_{hold} = 50 μA to 900 μA, as labeled.

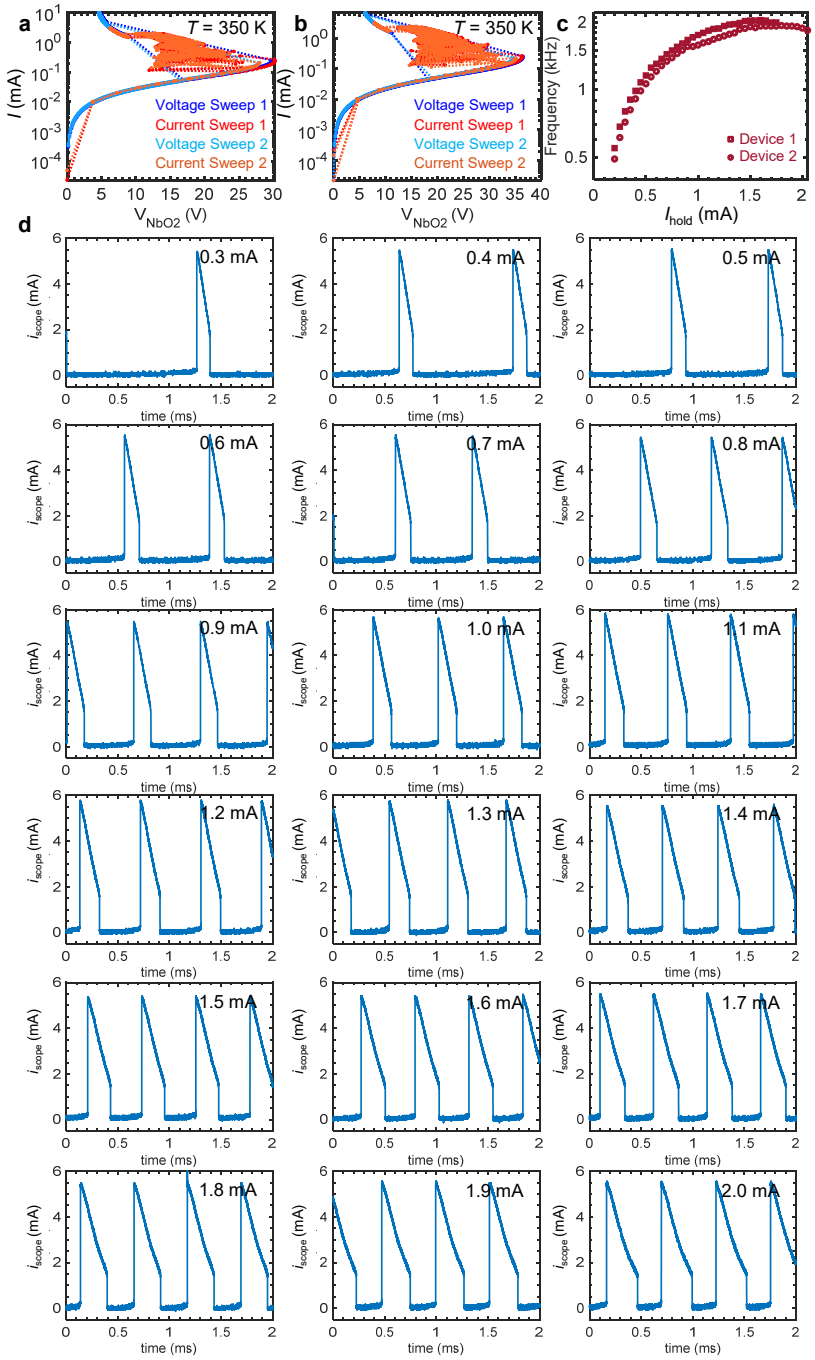

Fig. S4. Current oscillations measured in NbO_2 devices at 350 K with a 5.1 kΩ compliance resistor. Quasi-DC switching measured via dual voltage-controlled sweeps (blue and light blue) and current-controlled sweeps (red and orange, in fast measurement mode) in **a,** Device 1: 3 (L) × 4 (W) µm and **b,** Device 2: 4 (L) × 4 (W) µm. Voltage sweep 1 (blue) is performed in the pristine state and voltage sweep 2 (light blue) is taken after performing current sweep 1 (red), showing no burn-in in the device switching voltage when current-controlled sweeps are performed at elevated ambient temperatures due to the reduced switching voltages. **c,** Oscillation frequency versus current value (I_{hold}) when the devices are held in different regions within the NDR state. **c,** Corresponding current oscillations measured in Device 2 at different current values, I_{hold} = 0.3 mA to 2 mA, as labeled.

2. Measurement Setup for Simultaneous Electro-Optical Oscillations

The simultaneous electro-optical measurements were performed by coupling an ultra-sensitive Si photomultiplier (LYNX-A-33-050-T1-A) through a sapphire optical window with the wire-bonded NbO_2 devices. For the electrical setup, the devices were switched in a Nextron microprobe system under vacuum at $<10^{-2}$ Torr and a 5.1 kΩ compliance resistor in series. The Si photomultiplier was biased using a 5 V DC source to maximize its gain. To record the electro-optical oscillations, a Keysight InfiniiVision MSOX3024T oscilloscope was used with a 50 Ω input impedance in series with the device (for measuring device current) and a 1 MΩ input impedance in parallel to the photodetector (for measuring the photodetector voltage). A low-pass electrical filter (EF502 with passband frequency ≤ 100 kHz) was used to capture the photodetector voltage oscillations, which were also averaged over 20 windows, to maximize the signal-to-noise ratio. The setup is shown in **Supplementary Fig. S5a** while the results obtained are displayed in **Supplementary Fig. S6**.

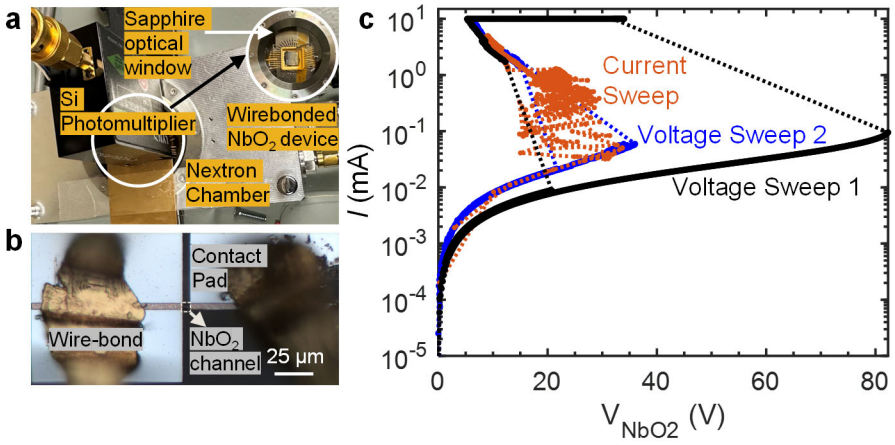

Fig. S5. Measurement of electro-optical neuronal activity in NbO_2 devices. **a,** Experimental setup for measuring simultaneous electro-optical oscillations displaying wire-bonded NbO_2 devices (circular inset) in a Nextron microprobe chamber under vacuum. The Si photomultiplier was aligned with the device of interest through a sapphire optical window. **b,** Optical image of a 5 μm long wire-bonded NbO_2 device whose electro-optical activity is displayed in main text **Figs. 2d** and **e**. **c,** Quasi-DC switching for the same device measured via dual voltage-controlled sweeps (black, voltage sweep 1 performed in pristine state and blue, voltage sweep 2 performed after the current sweep) and current-controlled sweeps (red) at room temperature ambient. Devices suffer more burn-in (*e.g.* compared to **Supplementary Figs. S1** and **S4**) when *current*-controlled sweeps are performed at *room temperature ambient* due to the very high switching voltages involved.

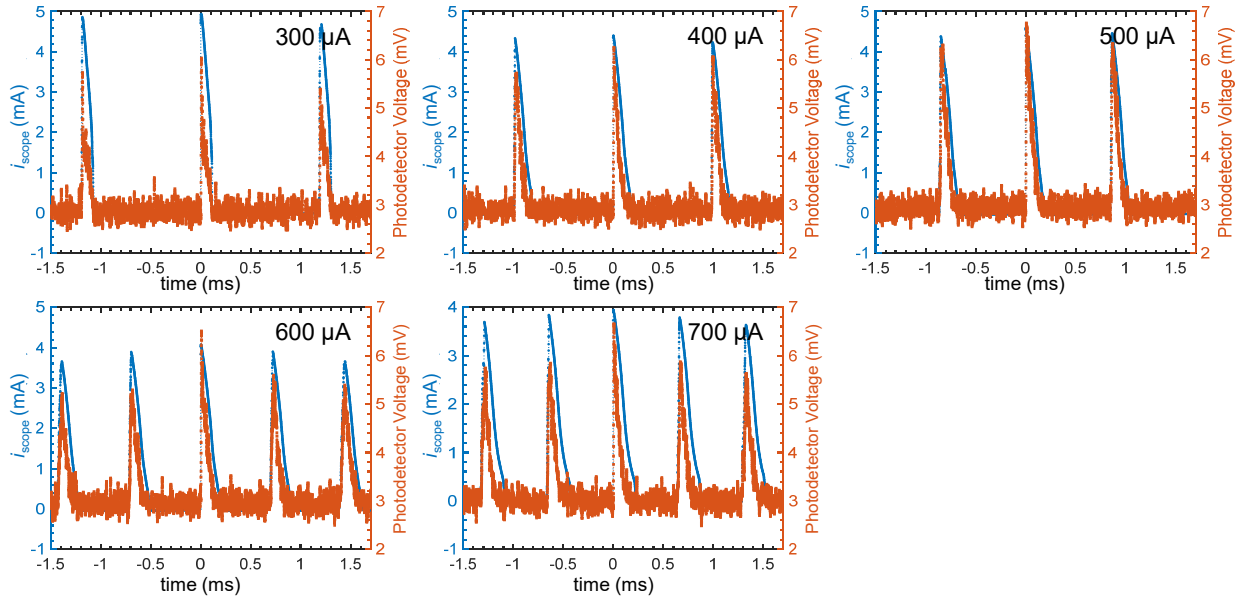

Fig. S6. Simultaneous electro-optical neuronal behavior measured in a 5 µm long wire-bonded NbO_2 device (shown in **Supplementary Fig. S5a**, **b**) biased at different regions (I_{hold} = 300 µA to 700 µA, as labeled) of the negative differential resistance (NDR) state (**Supplementary Fig. S5c**).

3. *Operando* Optical Microscopy for Varying Bias and Device Dimensions

All optical microscopy images and **Supplementary Video 1** were taken using a Hitachi KP-D20A CCD color camera, mounted on top of the optical microscope used with our Janis probe station. The magnification of the microscope and all camera controls were kept fixed during the experiment. No color corrections have been performed on the images shown in this work.

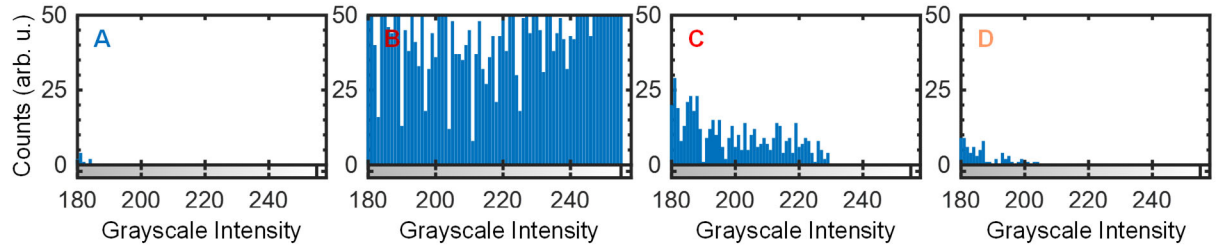

Fig. S7. Histogram plot of the pixel counts versus grayscale intensity for each optical image in **Fig. 2c**. Similar to **Fig. 2c**, each plot corresponds to a different bias state, A: high-resistance state, B: threshold switching (transient overshoot), C-D: low-resistance state (higher and lower current). The grayscale intensity represents the brightness of each pixel in a grayscale image and ranges from 0 (black) to 255 (white), although only intensity values above 180 are shown for clarity here. Similarly, the pixel count in this plot has also been cut off at 50; the highest pixel count is > 3000 measured for 'B' at 255 (not shown here), which is expected since the observed light emission is brightest under this bias state.

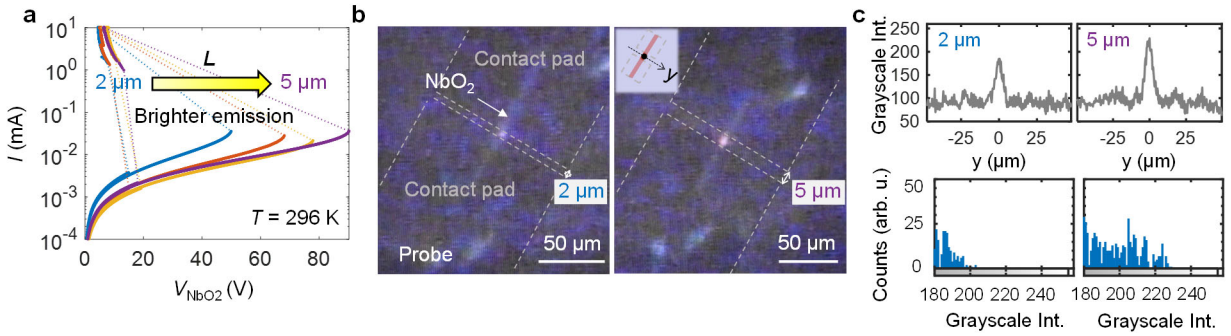

Fig S8. *Operando* imaging of light emission from NbO_2 devices of varying device length, L. **a,** Quasi-DC characterization of 3 μm wide NbO_2 devices with L varying from 2 to 5 μm showing increasing bias voltages required to achieve threshold switching. **b,** *Operando* images taken for $L \approx 2$ μm and $L \approx 5$ μm where the emission appears brighter for the device with a longer L and thereby higher switching voltage, V_{IMT}. These images were taken during threshold switching, similar to 'B' in **Fig. 2c**. **c,** Grayscale pixel intensity transverse to the NbO_2 strip ($y = 0$ approximately at mid-point). The right panel inset in b displays the y-axis in the context of the device schematic. The bottom panel shows the corresponding histogram plots of the pixel counts versus grayscale intensity, depicting higher counts at the brighter intensity values for $L \approx 5$ μm.

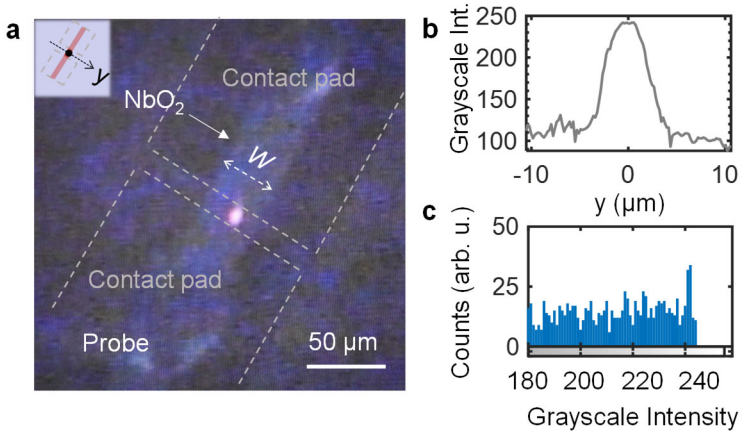

Fig S9. a, *Operando* images taken for a wide NbO_2 device with $W \approx 25$ μm, depicting the occurrence of light emission near the middle of the NbO_2 channel. **b,** Grayscale pixel intensity transverse to the NbO_2 strip ($y = 0$ approximately at mid-point). The inset in **a** displays the y-axis in the context of the device schematic. The plot represents brighter pixels only in the center of the NbO_2 channel. **c,** Corresponding histogram plot of the pixel counts versus grayscale intensity.

4. Pre- and Post-electrical Switching Characterization, and Temperature Dependence of NbO_2 devices

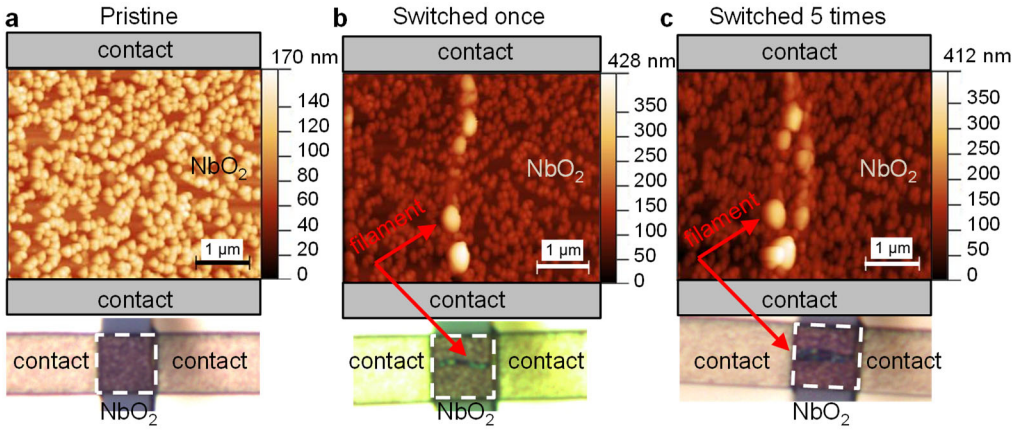

Fig. S10. Atomic force micrographs (AFMs) and optical images of a 5 μm long NbO_2 device in **a,** pristine state, **b,** after 1, and **c,** after 5 electrical switching cycles showing the formation of a filament track upon first switching which grows upon subsequent switching cycles. These AFMs were taken on devices capped with 35 nm thick SiN_x.

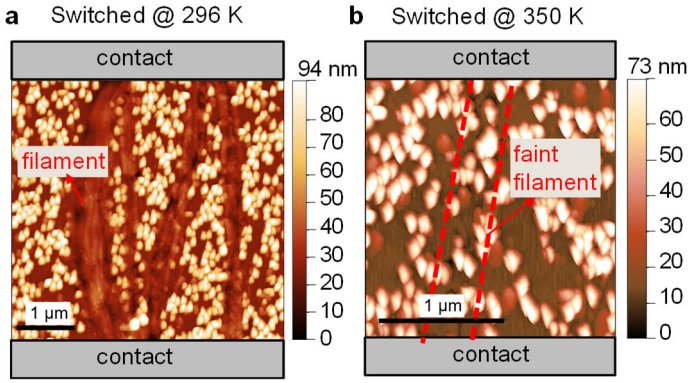

Fig. S11. AFMs of 4 μm long NbO_2 devices each switched *only* at **a,** T = 293 K and **b,** 350 K ambient temperature. The device switched at 350 K does not display clear filamentary tracks and did not exhibit detectable light emission using the visible range optical microscopy setup in **Fig. 2a** for this channel length.

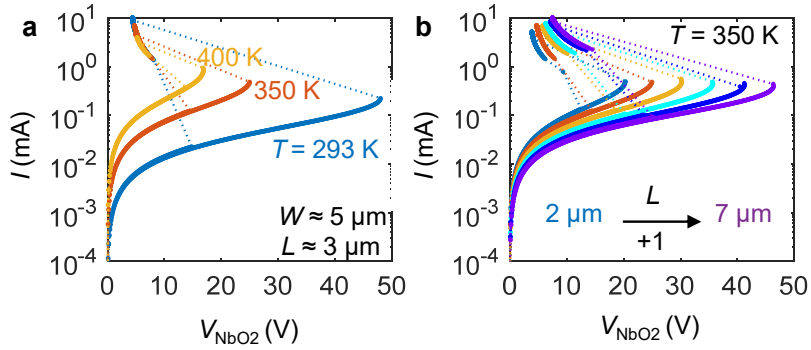

Fig. S12. Measured, voltage-driven quasi-DC behavior of NbO_2 devices with **a,** L = 3 μm at different ambient temperatures; light emission is observed only at 293 K ambient. **b,** Measured devices with varying channel length L at 350 K ambient temperature; light emission is observed for $L \geq 5$ μm.

Devices that were switched only at a higher ambient temperature did not show the formation of permanent filament tracks (**Supplementary Fig. S11**), possibly because there is less localized heating at higher ambient temperatures due to more parallel current leakage paths. Light emission under these conditions was also absent. This is corroborated by the decrease in V_{IMT} at higher ambient temperatures for the same device (same L), because less self-heating and lower input power are required to achieve threshold switching (**Supplementary Fig. S12**).

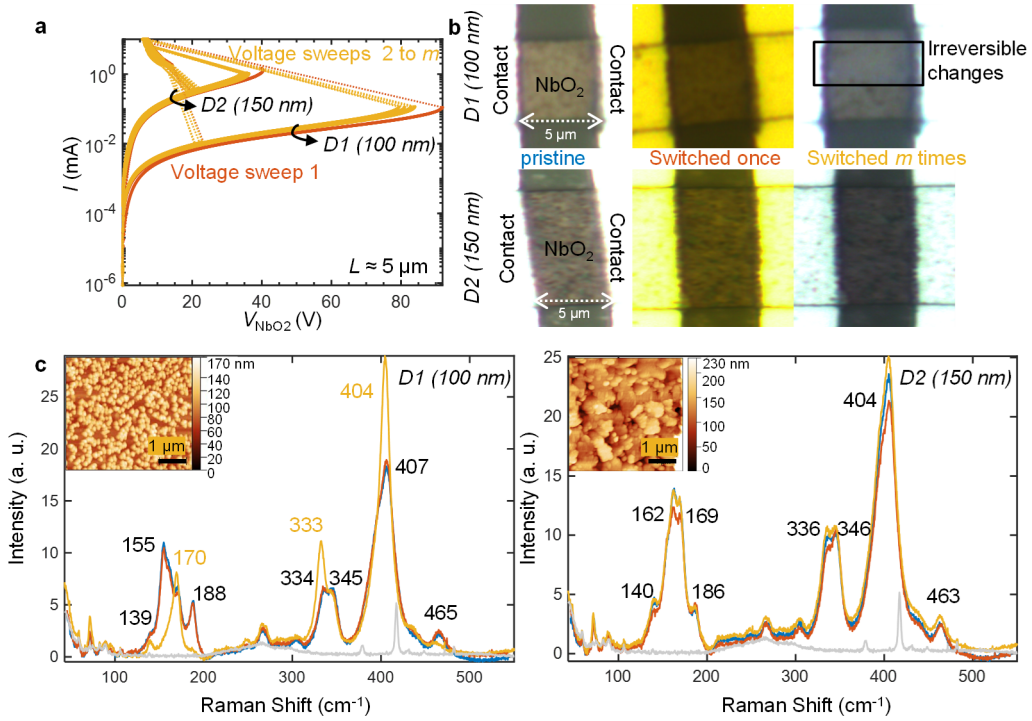

Fig. S13. Pre- and post-switching Raman characterization of NbO_2 devices labeled D1 (L = 5 µm, W = 5 µm) on chip 3 (100 nm thick NbO_2 film on 1 mm sapphire substrate, identical to chip 2) and D2 (L = 5 µm, W = 15 µm) on chip 1 (150 nm thick NbO_2 film on 0.5 mm sapphire substrate). **a,** Multiple dual voltage-controlled sweeps performed on D1 (m = 5 sweeps) and D2 (m = 20 sweeps) showing the usual burn-in during sweep 1 (red). Sweeps 2 to m are in yellow. Devices with similar channel lengths on chip 1 have substantially lower switching voltages. Light emission was observed for both devices during each resistive switching. **b,** Optical images of D1 and D2 in pristine state (blue), after the first switching (red), and after m switching cycles (yellow). Some irreversible changes are seen in the D1 channel after m = 5 switching cycles, but no changes are observed in D2 up to m = 20 switching cycles, possibly due to the lower channel temperatures from the lower switching voltages. **c,** Raman spectra taken on D1 and D2 in the pristine state (blue), after the first switching (red), and after m switching cycles (yellow) in approximately the same spot (tentative center of the NbO_2 strip where filament commonly forms). No changes in the spectra are seen upon the first resistive switching for either device (blue vs. red). Some shifts in the Raman peaks are observed for D1 after m = 5 voltage sweeps, which are not observed for D2 up to m = 20 switching cycles. The shifts observed in D1 are possibly due to subtle crystallographic and/or stoichiometric changes upon multiple switching. The gray Raman spectra correspond to the bare sapphire substrate. Insets show AFM mapping of the films in their pristine states (before switching) revealing their different topology. Although the growth conditions were identical, different substrate thickness could have caused minute changes in the resulting film properties.

The Raman spectroscopy measurements in **Supplementary Fig. S13** were performed using a HORIBA Scientific LabRAM HR Evolution spectrometer (532 nm laser, 376 nm spot size, 13.1 mW total laser power, 1800 l/mm grating) with 1.38 mW laser power, 10 s acquisition time, and 30 accumulations at room temperature ambient.

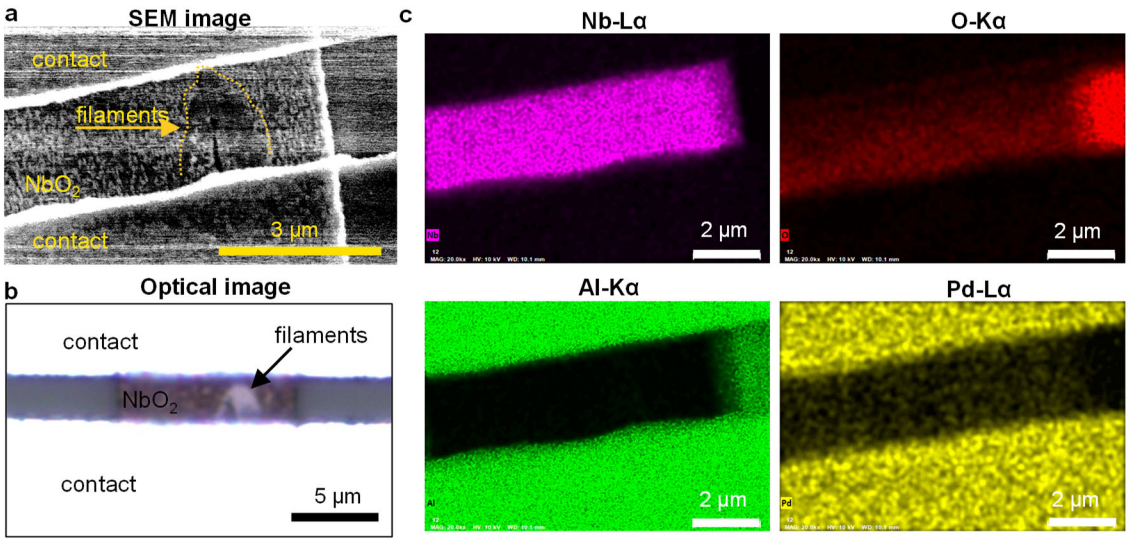

Fig. S14. Characterization of a 3 µm × 10 µm NbO_2 device after electrical switching. **a,** Top-down scanning electron microscopy (SEM) and **b,** optical image of the device after dual-voltage-controlled sweep showing filamentary track formation. **c,** Top-down energy-dispersive X-ray spectroscopy (EDS) elemental maps of Nb, O, Al and Pd. No difference in Nb or O maps is observed in the NbO_2 channel, where filamentary tracks are seen in **a** and **b**, to suggest changes in stoichiometry of the NbO_2 upon switching. Images were taken on a Thermo Fisher Scientific Apreo S LoVac SEM with an acceleration voltage of 10 kV and working distance of 10.1 mm.

5. Raman Thermometry Characterization of NbO_2 Devices

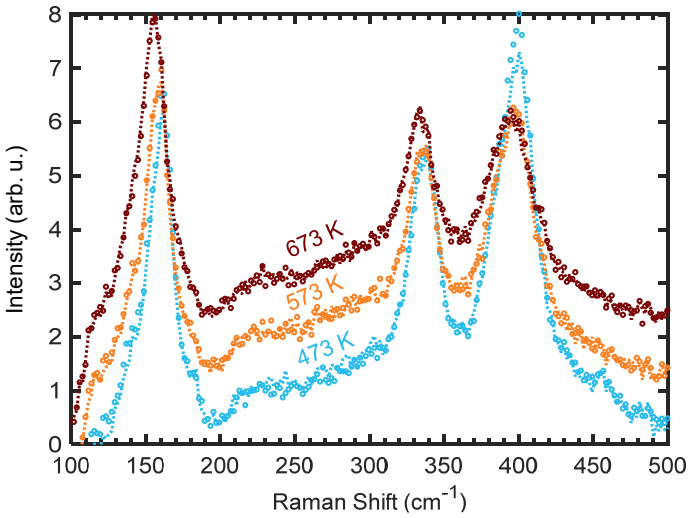

Fig. S15. Raman spectra taken on a 100 nm thick NbO_2 film at 473 K (blue), 573 K (orange), and 673 K (dark maroon) stage temperatures, arbitrarily stacked for ease of plotting. For each temperature, the round markers represent the first instance of Raman spectrum taken at that temperature. On the other hand, the dotted line represents a second instance of the spectrum taken at the same temperature, *after* having heated the film 100 K higher and subsequently cooled back down to the temperature of interest. The coincidence of the two spectra at each temperature confirms no temperature-induced permanent changes in the NbO_2 Raman modes at least up to 673 K.

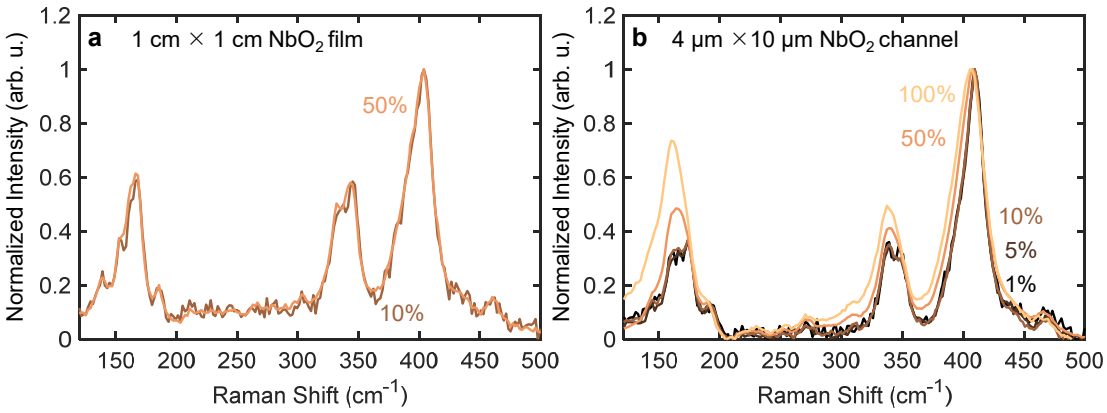

Fig. S16. Effect of laser power used in Raman spectroscopy on NbO_2 Raman modes at 303 K stage temperature. **a,** Raman spectra of a 100 nm thick NbO_2 film measuring ~1 cm × 1 cm using 10% (brown) versus 50% (orange) laser power. The coincidence of the two spectra confirms no substantial heating due to 50% laser power in the blanket film and no additional Raman shifts for the acquisition time used due to laser heating. To avail a higher signal-to-noise (SNR) ratio and minimize acquisition time, 50% laser power was used for performing Raman spectroscopy on NbO_2 films. **b,** Raman spectra taken on a 4 μm ×10 μm NbO_2 (100 nm thick) device using 1 % (black) to 100 % (light orange) laser powers. Spectra taken at laser power > 10 % display an increasing redshift similar to that caused by increasing stage temperatures **(Fig. 3a**), indicating substantial heating caused by the laser. Thus, a laser power of 10% was chosen for performing Raman spectroscopy on NbO_2 devices for which no red shift was observed (with respect to 1% laser power) in order to maximize SNR.

A 50% laser power was used for temperature-dependent Raman on NbO_2 blanket films and was reduced to 10% for bias-dependent measurements to prevent substantial heating in the NbO_2 device channel as well as any changes in the electrical characteristics of the NbO_2 devices due to laser heating. The laser power was thus optimized to ensure that the measured Raman shift was due to Joule-heating only while simultaneously maximizing the observed counts (**Supplementary Fig. S16**).

Table S1. Measured optical power for laser power percentages used in Raman thermometry.

Laser power (%)	Optical power measured (mW)
100	9.28
50	5.32
10	0.81
5	0.40
1	0.15

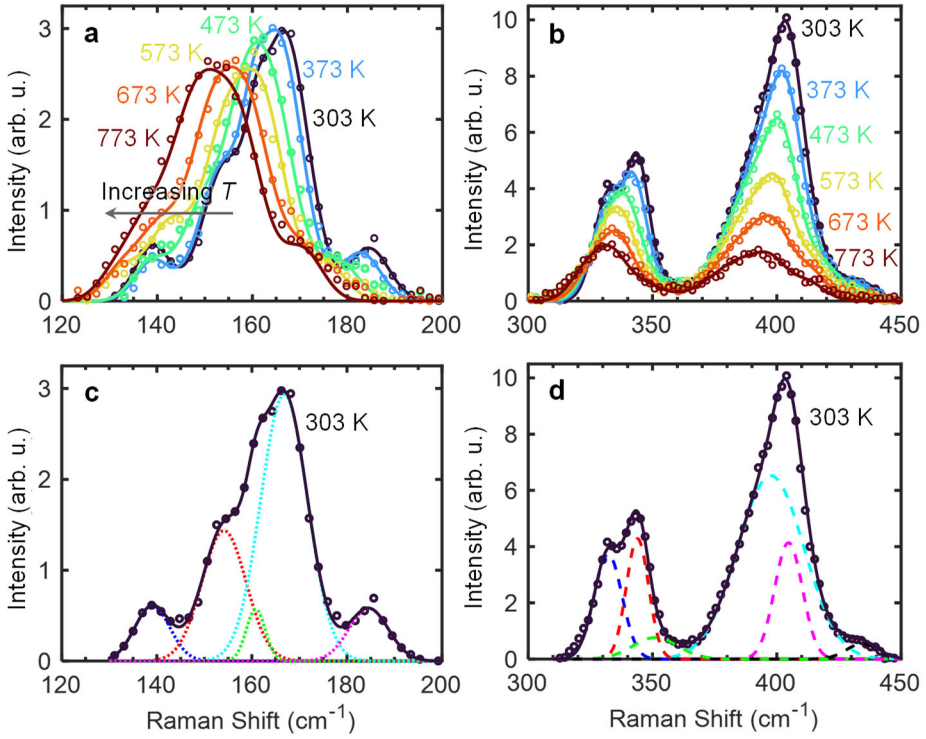

Fig. S17. Gaussian peak fitting for Raman spectra of NbO_2 films. Measured (round markers) and fitted (solid lines) NbO_2 Raman spectra between **a,** 120 to 200 cm^{-1} and **b,** 300 to 450 cm^{-1} shifts for increasing stage temperatures. **c,** and **d,** show the peak decomposition of the respective spectra only at 303 K stage temperature. The primary Raman mode near 400 cm^{-1} (dashed cyan curve in **d**) was selected for thermometry on the NbO_2 devices because only its peak position varied with temperature (and with voltage bias, as in **Supplementary Fig. S18**) while all other parameters (including width and number of peaks needed for fitting the Raman mode) were temperature (and bias) independent.

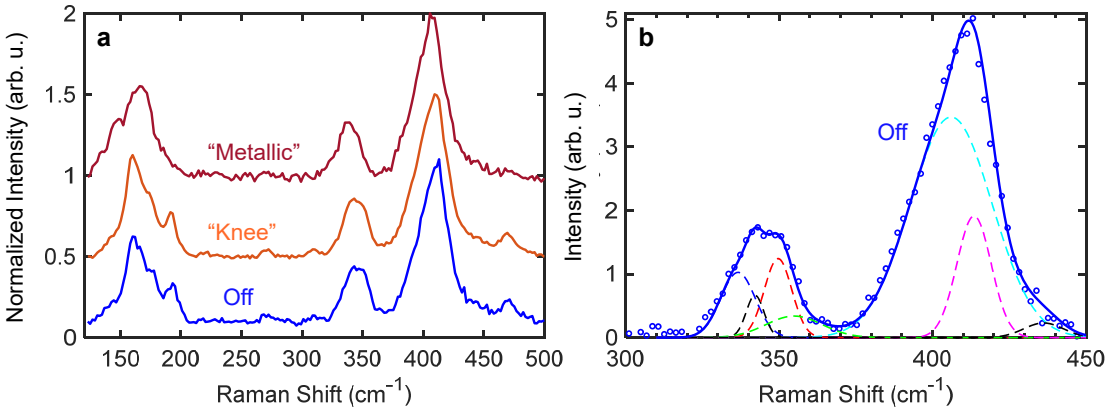

Fig. S18. Raman spectroscopy on a 5 µm long NbO_2 device for different electrical biases. **a,** Raman spectra taken on the NbO_2 channel when device was held under different electrical biases as shown in **Fig. 3c** inset and referred to as off, "knee" of the *I–V* curve, and "metallic" bias states. **b,** Experimental data (round markers) and peak decomposition using Gaussian fits (lines) for the off state between 300 and 450 cm^{-1}. The primary Raman mode near 400 cm^{-1} (dashed cyan curve) was used to perform Raman thermometry since only its peak position varied with bias (and temperature), while all other parameters were bias (and temperature) independent. The solid blue line is the sum of the (decomposed) dashed lines.

Table S2. Extracted *in-situ* channel temperatures for our NbO_2 device under different electrical biases. The second column lists the bias values for the two states labeled "knee" of the *I–V* and "metallic" in **Fig. 3c** inset. The third column shows the shift in the peak position of the primary Raman mode near 400 cm^{-1} for the two bias states calculated with respect to the "off" state (dashed cyan curve in **Supplementary Fig. S18b**). The fourth column shows the estimated temperature rise in the NbO_2 channel with respect to room temperature extracted using the red-shift rate calculated for this mode: -0.021 ± 0.004 cm^{-1}/K (**Fig. 3b** inset).

Bias State	V_s, I	ΔRaman shift (w.r.t. "off")	ΔTemp. (above room temp.)
"knee"	70 V, 70 µA	1.39 cm^{-1}	**69 ± 13 K**
"metallic"	88 V, 16 mA	4.07 cm^{-1}	**201 ± 38 K**

6. Finite Element Simulations of Local Temperatures

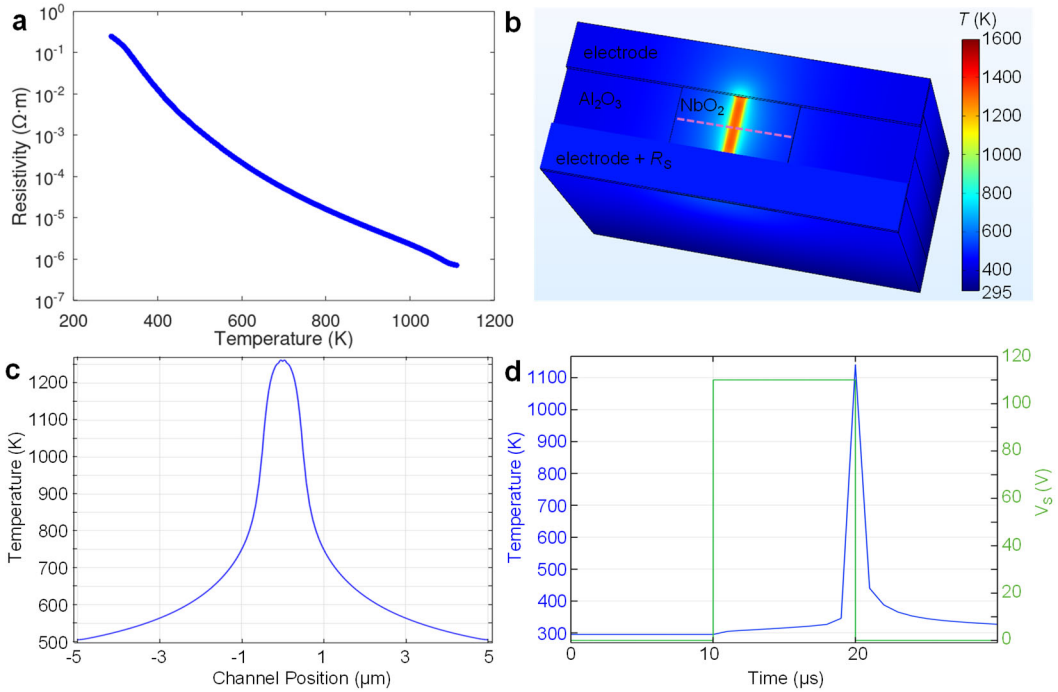

Fig. S19. Simulated temperature of an NbO_2 device in the metallic state. **a,** Temperature-dependent resistivity used in the model, based on measured resistivity near room temperature combined with data from literature[1, 2]. **b,** Simulated steady-state surface temperature in the metallic state at a bias of V_S = 90 V showing a ~1 μm wide high temperature filament in the center of the channel (L = 5 μm, W = 10 μm, R_S = 5 kΩ). The surface temperature profile on one of the electrodes is obscured by the series resistor block. **c,** Temperature along the NbO_2 channel width following the pink dashed line in **b**, taken midway along the channel length and in the center of the film depth (i.e., 50 nm below the surface of the 100 nm film). **d,** Transient response of peak temperature (blue curve) in the filament as a 110 V voltage pulse (green curve) is applied to the device.

We used a three-dimensional finite element model built in COMSOL Multiphysics to obtain a rough estimate for the steady state and transient filament temperature in our NbO_2 devices. The model self-consistently solves for both the temperature and electric field distributions within the device and includes the series resistor used in experiments to protect devices from failure.

The simulated device has a similar structure to the schematic in main text **Fig. 2a**, with an NbO_2 channel of length L = 5 μm and width W = 10 μm. We used a temperature dependent resistivity for the NbO_2 shown in **Fig. S19a**, which is based on literature curves[1, 2] that have been scaled to match the measured room temperature resistivity of our films. The resistivity was discretized in temperature to a 0.1 K resolution with nearest neighbor interpolation, rather than a linear interpolation or continuous function, to improve convergence. No hysteresis was included in the insulator-metal transition (IMT).

The modeled contact pads and substrate extend 10 μm on either side of the NbO_2 channel, and a depth of 20 μm was used for the modeled Al_2O_3 substrate. We used thermal conductivity of 5 $Wm^{-1}K^{-1}$, 35 W $m^{-1}K^{-1}$, and 70 W $m^{-1}K^{-1}$ for NbO_2, Al_2O_3, and the metal contacts, respectively. For transient simulations, we used thermal heat capacity of 480 J kg^{-1} K^{-1}, 710 J kg^{-1} K^{-1}, and 244 J kg^{-1} K^{-1} for NbO_2, Al_2O_3, and the metal contacts, respectively. The series resistor was included as a layer which is thermally decoupled from the system and whose total resistance is 5 kΩ, placed on top of one of the contact pads. We included a thermal boundary resistance at the contacts/Al_2O_3 and contacts/NbO_2 interfaces of 10^{-8} m^2K/W, and at the NbO_2/Al_2O_3 interfaces of 0.8×10^{-8} m^2K/W. The electrical contact resistivity to the NbO_2 is set to 10^{-8} $\Omega \cdot m^2$ at room temperature and is scaled with temperature in the same way as the NbO_2 resistivity. In steady state, the model was solved with a direct segregated approach described in more detail in Bohaichuk *et al.*[3] Temperature was solved first followed by electric potential, with damping factors of 0.2 and 0.4, respectively.

The switching point of the device was found to be around V_S = 85 V at a current of 134 μA. In steady-state at V_S = 90 V, shown in **Fig. S19b** and **S19c**, the model shows the formation of a hot low-resistance filament in the center of the device with a width of ~1 μm and a maximum temperature of ~1250 K. We note that this temperature is well below the melting point of bulk NbO_2, ~2190 K, so we do not expect our films to be molten in steady state, but they may still undergo some form of re-crystallization or annealing during operation. The exact temperatures and switching conditions of the device depend on several electrical and thermal parameters that are not well known and are difficult to measure in these films, most significantly the resistivity at high temperatures. Thus, the values presented here are merely an estimate.

We also examined the transient evolution of surface temperatures in the simulated NbO_2 device in response to a step voltage of 110 V applied for 10 μs, shown in **Fig. S19d**. The relative tolerance for the transient solution was 0.001. **Fig. S19d** shows that the peak temperature of the metallic filament remains well below the melting point of bulk NbO_2, similar to the steady-state results.

7. Electro-optical Power Conversion Estimation

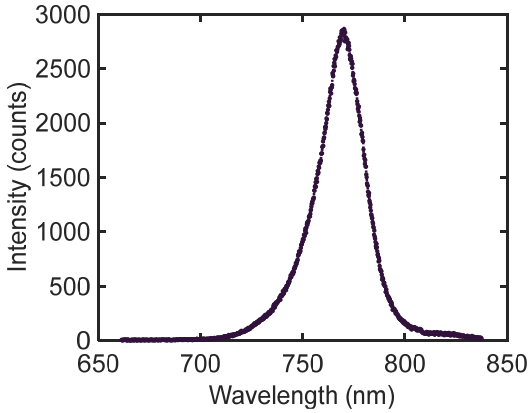

Fig. S20. Spectral response of a standard 780 nm LED measured using the spectrometer used for emission measurements shown in **Fig. 4a** under the same acquisition settings.

To estimate the electro-optical power conversion efficiency of our NbO_2 device in **Fig. 4a**, we used a standard 780 nm LED to calibrate our spectrometer. The spectral response of this LED taken at 15 mA and 1.3 V electrical bias (using the same spectral settings as used for our emission measurements) is displayed in **Supplementary Fig. S20**.

The corresponding optical power of the LED at 780 nm was measured to be 800 nW and consequently, the number of photons emitted per second was calculated. Thus, the measured intensity counts of the spectrometer was calibrated to number of photons emitted per second. This calibration ratio was then used to calculate the number of photons emitted per second at 816 nm for our NbO_2 device whose spectral response is shown in **Fig. 4a** and peaks around that wavenumber.

Supplementary References

1. Shibuya, K. & Sawa, A. Epitaxial growth and polarized Raman scattering of niobium dioxide films. *AIP Adv.* **12,** 055103 (2022).
2. Seta, K. & Naito, K. Calorimetric study of the phase-transition in doped NbO_2. *J. Chem. Thermodyn.* **14,** 937-949 (1982).
3. Bohaichuk, S. M. et al. Localized triggering of the insulator-metal transition in VO_2 using a single carbon nanotube. *ACS Nano* **13,** 11070-11077 (2019).